

# PHOTONICS Research

## Optical Vernier sampling using a dual-comb-swept laser to solve distance aliasing

SEONGJIN BAK,<sup>†</sup> GYEONG HUN KIM,<sup>†</sup> HANSOL JANG, AND CHANG-SEOK KIM<sup>\*</sup>

Department of Cogno-Mechatronics Engineering, Pusan National University, Busan 46241, Republic of Korea

<sup>\*</sup>Corresponding author: ckim@pusan.ac.kr

Received 27 November 2020; revised 9 February 2021; accepted 21 February 2021; posted 22 February 2021 (Doc. ID 416025); published 15 April 2021

Optical interferometry using comb-swept lasers has the advantage of efficiently reducing the acquisition bandwidth for high-speed and long-range detection. However, in general, the use of a comb-swept laser involves a critical limitation in that the absolute distance cannot be measured, and, thus, multiple layers cannot be distinguished when measuring each position. This is because of the distance ambiguity induced by optical aliasing, in which there is periodic repetition of the frequency of an interferometric signal owing to discrete spectral sweeping, which does not occur in conventional optical interferometry that uses a continuous swept laser. In this paper, we introduce an optical Vernier sampling method using a dual-comb-swept laser to measure the absolute distances in a multi-layer target. For this, we designed a new type of dual-comb-swept laser to include two different free spectral ranges (FSRs) in separated wavelength bands to provide a stable lasing condition. Using a principle similar to that of a Vernier caliper for length measurement, the two different FSRs can be used to recover a higher frequency of an optical interferometric signal to measure longer distances from different layers in a target. Using the dual-comb-swept laser in optical interferometry, we solved the optical aliasing issue and measured the absolute distances of three layers separated over 83 mm using a point-scanning imaging setup and the simultaneous absolute distance of the top surfaces separated over 45 mm using a full-field imaging setup at 14 and 8 times lower acquisition bandwidth than a conventional continuous swept laser that is based on optical interferometry. © 2021 Chinese Laser Press

<https://doi.org/10.1364/PRJ.416025>

### 1. INTRODUCTION

Optical interferometry is a well-established method for measuring distances with high accuracy and long range and in multiple layers of targets [1–3]. Currently, optical coherence tomography (OCT) is employed in biomedical imaging and industrial inspection applications [4–8]. Recently, the high-speed A-scan at a deep depth using a swept-source OCT (SS-OCT) system has become possible owing to the development of a continuous swept laser with a high sweep rate and long coherence length [9–15]. By employing a state-of-the-art continuous swept laser, a deeper imaging depth and faster imaging speed can be implemented. However, this will cause a considerable amount of burden on electric detectors with a limited electrical bandwidth [9,11,16].

Recently, a solution was suggested for deeper and faster imaging without using a faster detector, i.e., using a comb-swept laser instead of a conventional continuous swept laser [5,9,11,17–19]:

$$D = \frac{T \cdot c \cdot f}{2B}. \quad (1)$$

Equation (1) [3,20] gives the relationship among the measured distance ( $D$ ), time period of the swept-source ( $T$ ), speed of light ( $c$ ), frequency of the interferometric signal ( $f$ ), and spectral bandwidth of the swept-source ( $B$ ). Most of the factors in Eq. (1), except  $f$ , are fixed values during the measurement of varying distances under given measurement conditions. This implies that  $D$  can be proportionally changed by varying  $f$ , and, accordingly, the measurement of a large value of  $D$  must correspond to a large value of  $f$ . A faster continuous swept laser with a shorter time period,  $T$ , will induce a larger value of  $f$  for the same distance,  $D$ . Therefore, the longer coherence length and faster sweep rate of a continuous swept laser require a much faster detector and wider acquisition bandwidth in a conventional SS-OCT system. Therefore, comb-swept lasers have recently been investigated for their use in the SS-OCT system to capitalize on the advantage of reducing the electrical bandwidth of detecting devices. This feature of comb-swept lasers provides a periodic repetition of  $f$  as the target distance increases continuously [9,17–19]. The periodic repetition has only limited values below the frequency limit of the interferometric signal,  $f_{\text{lim}}$ . As a result of the limited value of the measured  $f$ ,  $D$  also

has only periodic repetition and a limited value. This periodic repetition of the  $D$  is called distance aliasing and is induced from the discrete distribution of the spectrum over the wavelength domain of the comb-swept laser output [21].

Thus, solving this distance aliasing has been a challenging issue when conducting optical interferometry using comb-swept lasers. Recently, a dual-reference method was suggested for measuring the absolute distance in the first aliasing order, but the dual-reference method cannot measure the higher order of absolute distance after the first order [18]. Another method for resolving the absolute depth was suggested using a degenerated frequency comb that resolves an absolute depth of approximately 10 mm, but this degenerated frequency comb method is expected to be difficult to adapt in a dispersive medium or longer-range measurement because the method detects a chirped point spread function (PSF) as increasing the aliasing order [22]. In this paper, we introduce a dual-comb-swept laser that includes two different free spectral ranges (FSRs) for the incorporation of the optical Vernier sampling method [16]. When conducting length measurement using a Vernier caliper, two different scales of the ruler are used. Using these two scales, one can measure the length with accuracy much higher than that obtained using a normal one [23]. We applied this simple principle of the Vernier caliper to our

optical interferometry system consisting of a dual-comb-swept laser. Similar to the length measurement using a Vernier caliper, our novel method incorporates the optical Vernier sampling method and uses two different FSRs from a dual-comb-swept laser, which corresponds to different scales of the two rulers in a Vernier caliper. In this proposed optical Vernier sampling method, we can recover a much higher frequency of the original distance by combining two lower frequencies of each aliased interferometric signal [16].

## 2. PRINCIPLE AND EXPERIMENTAL SETUP

### A. Principle of the Optical Vernier Sampling Method

Figure 1 shows the principle of the optical Vernier sampling method using a dual-comb-swept laser for solving distance aliasing. As shown in Fig. 1(a), two different FSR values, namely,  $\text{FSR}_a$  and  $\text{FSR}_b$ , can be selected in a dual-comb-swept laser using comb A and comb B, respectively. The dual-comb-swept laser emits a serial comb line in the time domain. The flowing arrow paths of comb A and comb B are represented by the blue and red arrows, respectively, in Fig. 1. As shown in Fig. 1(b), the light from the dual-comb-swept laser with  $\text{FSR}_a$  and  $\text{FSR}_b$  passes through an optical interferometer. Here, the light from combs A and B enters a beam splitter (BS) and passes through

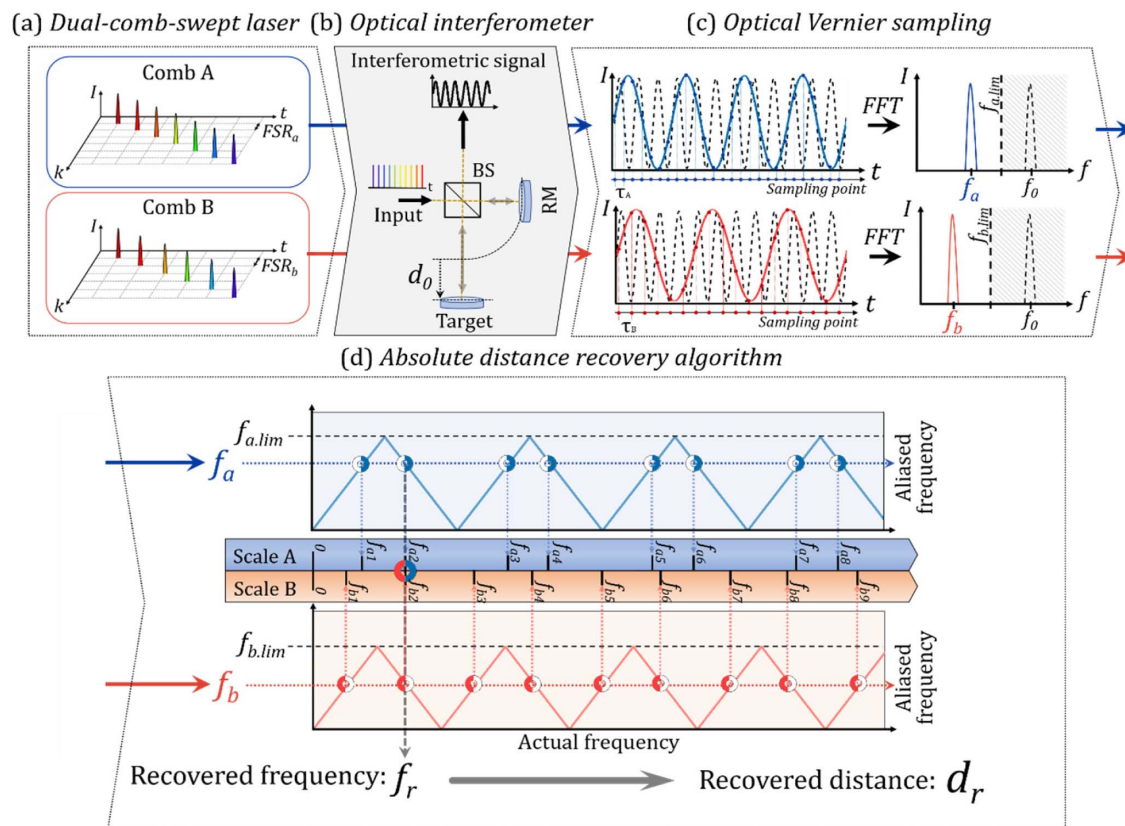


**Fig. 1.** Principle of the optical Vernier sampling method for solving distance aliasing. (a) A dual-comb-swept laser using comb A and comb B shows two different FSR values, namely,  $\text{FSR}_a$  and  $\text{FSR}_b$ , respectively. (b) Optical interferometer to measure the absolute distance of the target. BS, beam splitter; RM, reference mirror. (c) Actual interferometric signal using a continuous swept laser with a frequency of  $f_0$  (dashed line), and sampled interferometric signals using a proposed dual-comb-swept laser using comb A to indicate the aliasing frequency of  $f_a$  (blue line) and using comb B to indicate the aliasing frequency of  $f_b$  (red line), respectively. (d) Absolute distance recovery algorithm by measuring two aliasing frequencies of  $f_a$  and  $f_b$  together.

each path of the reference mirror (RM) and target separately. The two paths of the target and RM have an absolute distance of  $d_0$ , which induces an interferometric signal. The black dashed curves plotted on the left side of Fig. 1(c) are the actual interferometric signals obtained using a continuous swept laser, and they have an  $f$  of  $f_0$  for an absolute distance of  $d_0$ . The gray hatched area on the right side of Fig. 1(c) indicates the fast Fourier transform (FFT) spectra, representing the  $f_0$  for the light coming from the continuous swept laser.

In comparison, for the same  $d_0$ , but for the light from the dual-comb-swept laser using combs A and B, the discrete spectral sweeping of the laser output generates an  $f$  with only limited values below certain levels  $f_{a,\text{lim}}$  and  $f_{b,\text{lim}}$ , respectively, which are determined by  $\text{FSR}_a$  and  $\text{FSR}_b$  and represented by the black dashed lines in Fig. 1(c). The blue and red solid curves plotted as a function of time are the measured aliased interferometric signals with combs A and B, respectively. The aliased interferometric signal caused different intervals of sampling points of each comb A and comb B. The sampling intervals  $\tau_A$  and  $\tau_B$  correspond to the FSRs of comb A and comb B, respectively. The FFT spectra of both interferometric signals correspond to the  $f$  using comb A of  $f_a$  and using comb B of  $f_b$ . As  $d_0$  varies continuously, the aliased frequencies of  $f_a$  and  $f_b$  periodically increase and decrease below  $f_{a,\text{lim}}$  and  $f_{b,\text{lim}}$  for the light from the dual-comb-swept laser using combs A and B, respectively.

As shown in Fig. 1(d), the FFT peak values of  $f_a$  and  $f_b$  are processed using the absolute distance recovery algorithm, which includes the relationship between the actual frequency of the continuous swept laser and two aliased frequencies measured using the dual-comb-swept laser, as shown by the blue and red solid lines. When  $\text{FSR}_a$  is smaller than  $\text{FSR}_b$  for a dense comb A and sparse comb B, the frequency limit of the interferometric signal using comb A,  $f_{a,\text{lim}}$ , is higher than the frequency limit of the interferometric signal using comb B,  $f_{b,\text{lim}}$ , as indicated by the black dashed lines. When comb A is applied, the aliased frequency using comb A,  $f_a$ , corresponds to the different possible positions of the actual frequency, which are represented by the half-filled blue circles in the figure. However, when comb B is applied, the aliased frequency using comb B,  $f_b$ , also corresponds to different actual frequencies, which are represented by the half-filled red circles in the figure. Thus, using only a single measurement of the aliased frequency of  $f_a$  or  $f_b$ , it is impossible to find  $f_0$  and  $d_0$ .

However, when the measurement results of both  $f_a$  and  $f_b$  are used together, it is possible to determine  $f_r$  and  $d_r$ . Two different baselines of scales A and B can be used along with the two aliased frequencies. On these two different scales, a matching position between the two half-filled blue and red circles at a specific actual frequency position can be found. This matching position is the recovered frequency, which is represented by the completely filled blue–red circle. The recovered frequency,  $f_r$ , has a one-to-one correspondence with the pair of  $f_a$  and  $f_b$  with different orders for each aliasing order  $o_a$  and  $o_b$ , such that

$$f_r = (f_a; o_a, f_b; o_b), \quad (2)$$

where  $o_a$  and  $o_b$  represent the aliasing order using combs A and B, respectively. Thus, the recovered frequency,  $f_r$ , can be used

to reconstruct the recovered distance,  $d_r$ , using Eq. (1). This implies that the recovered distance,  $d_r$ , can also be represented with a bijective functional form, including the pair  $d_a$  and  $d_b$  with a different order for each aliasing order,  $o_a$  and  $o_b$ :

$$d_r = (d_a; o_a, d_b; o_b), \quad (3)$$

where  $d_a$  and  $d_b$  represent the aliased distance using combs A and B, respectively. Furthermore, each aliasing order of  $o_a$  and  $o_b$  represents data compression in the electrical bandwidth. A more detailed description [represented by Eq. (A1)] is provided in Appendix A.

## B. Experimental Setup

For the recovery algorithm that incorporates optical Vernier sampling, a novel design of a dual-comb-swept laser has been proposed, as shown in Fig. 2(a). The black line corresponds to the optical fiber part, whereas the red line corresponds to the free-space part. The light from the semiconductor optical amplifier (SOA) was collimated by collimator 1 (COL 1) to the free space and was separated by a dichroic mirror (DM), depending on its two wavelength bands. Because the total wavelength band of the SOA was from 768.8 to 812.5 nm, the spectral width of each wavelength band was tuned to be similar by controlling the incident angle of the free-space light into the DM. From a wavelength of approximately 790 nm, the longer wavelength band (band B) was filtered for light through the DM, whereas the shorter wavelength band (band A) was gathered from the light reflected by the DM. Each of the separated wavelength bands passed through etalon A and etalon B. Owing to the slightly different thickness of each etalon, both wavelength bands had slightly different comb spacings in their individual comb spectra. The comb lights of bands A and B were combined using the two input ports of the 50:50 optical coupler (OC). One output port of this OC was connected to the inside of the laser cavity, and the other was connected to the laser output. Along the inside of the laser cavity, a fiber Fabry–Perot tunable filter (FFP-TF) was installed to achieve controlled sweeping of a single wavelength during the total sweeping period, including that for bands A and B together. The discrete spectral sweeping with the two cascaded FSRs was generated by simply combining the continuous sweeping spectrum of the FFP-TF with the periodic comb spectra obtained after passing through etalons A and B. The FFP-TF was operated with a triangular function by an arbitrary function generator (AFG) and the maximum repetition rate is 100 Hz. In the case of sine function, the FFP-TF can operate with a higher repetition rate of several kilohertz (kHz). Repetition rate stability of the dual-comb-swept laser is related to mechanical dynamics of the FFP-TF during the wavelength sweep. The FFP-TF operates by AFG with a fine frequency resolution of 1  $\mu\text{Hz}$  and a low jitter of 35 ps. To achieve stable temperature conditions of FFP-TF, a thermo-electric cooler (TEC) was employed with a TEC controller (TEC CTRL). Inside the laser cavity, a polarization controller (PC) and an isolator (ISO) were used to achieve high lasing efficiency. By passing through a boosting optical amplifier (BOA), the output optical power was improved to approximately 20 mW, which was sufficient for applying to a full-field optical interferometry imaging setup with multiple pixels of a complementary metal oxide



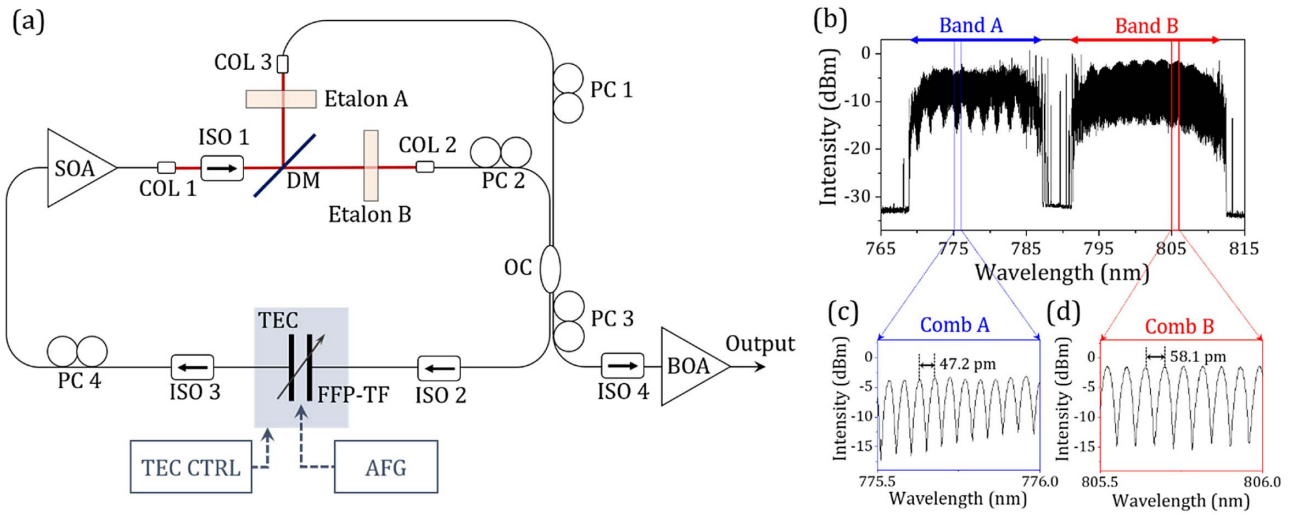


**Fig. 2.** (a) Setup of the dual-comb-swept laser. The black and red lines represent the fiber and free-space part, respectively. SOA, semiconductor optical amplifier; PC, polarization controller; COL, collimator; ISO, isolator; DM, dichroic mirror; OC, optical coupler; FFP-TF, fiber Fabry–Perot tunable filter; BOA, boosting optical amplifier; TEC, thermo-electric cooler; AFG, arbitrary function generator; TEC CTRL, TEC controller. (b) Optical spectrum of the peak hold mode obtained from the dual-comb-swept laser. Enlarged views of the spectra obtained using (c) comb A in the wavelength range of 775.5 to 776 nm and (d) comb B in the wavelength range of 805.5 to 806 nm.

semiconductor (CMOS) camera and with a point-scanning imaging setup equipped with a single photodetector for target measurements. The longitudinal mode of the laser cavity was measured to be  $\sim 21.3$  MHz in a static lasing (i.e., non-sweep) condition at 803.5 nm, corresponding to the cavity length of  $\sim 14$  m (in air):

$$\Delta f = \text{FSR} = \frac{c}{2n_e \cdot l_e}. \quad (4)$$

Equation (4) shows the comb spacing relationship among an FSR of a comb source ( $\Delta f$ ), the speed of light ( $c$ ), the refractive index of the etalon ( $n_e$ ), and the thickness of the etalon ( $l_e$ ) [11]. Because the designed thicknesses of etalons A and B are 4.3 and 3.8 mm, respectively, the designed FSRs of combs A and B sources are 47.5 pm (23.7 GHz) and 58.1 pm (26.8 GHz). The linewidths of etalons A and B are 2.13 pm and 2.41 pm, respectively, which correspond to  $\sim 1$  GHz. Therefore, as scanning the transmission window of FFP-TF, it is sufficient to generate a narrow comb-swept lasing output without the gain competition. Figure 2(b) shows the peak hold mode spectral data obtained from a dual-comb-swept laser, in which the spectra for both comb sources have been presented for bands A (a shorter wavelength band from 768.8 to 787.2 nm) and B (a longer wavelength band from 791.1 to 812.5 nm). Of note, the laser spectrum from 787.2 to 791.1 nm was not clearly generated because of the low lasing efficiency resulting from the limited sectioning between the free-space reflection and transmission in the DM. Figures 2(c) and 2(d) show the enlarged views of the comb A spectrum in the wavelength range from 775.5 to 776.0 nm and the comb B spectrum from 805.5 to 806.0 nm, respectively. The measured FSRs from the average of combs A and B sources are 47.2 and 58.1 pm, respectively, which are similar to the designed values. The high stability of

the dual-comb-swept laser can be guaranteed because the lasing of both comb sources is independently generated in the spectrally separated wavelength bands of A and B, respectively:

$$\Delta d = \frac{c}{2 \cdot \Delta f} = n_e \cdot l_e. \quad (5)$$

Equation (5) provides the numerical relation of the distance aliasing period ( $\Delta d$ ) obtained from comb-swept laser [9,11]. Factors  $n_e$  and  $l_e$  represent the refractive index and thickness of the etalon, respectively [19]. As illustrated in Figs. 1(a) and 1(c) above, compared to the sparse comb spacing (a larger value of  $\Delta f$ ) of the comb B source, the dense comb spacing (a smaller value of  $\Delta f$ ) of the comb A source can obtain more sampling points and higher frequency terms from the actual  $f$ ,  $f_0$ . This implies that the frequency limit of the interferometric signal,  $f_{a,\text{lim}}$ , is higher than  $f_{b,\text{lim}}$ , and, thus, the aliasing distance period,  $\Delta d_{a,\text{lim}}$ , is longer than  $\Delta d_{b,\text{lim}}$ . Using Eq. (5), the theoretical aliasing distance periods of combs A and B were calculated to be 6.350 and 5.600 mm, respectively. These values were utilized in the numerical simulation of the optical Vernier sampling.

### 3. RESULTS

By combining the two aliased frequencies with a dual-comb-swept laser, our novel optical Vernier sampling was verified by conducting the following tests. (i) PSF was measured, and the coherence length of the dual-comb-swept laser was determined. (ii) The recovered distance by the aliased distance using combs A and B was compared with that obtained from the numerical simulation by employing Eq. (5), and the analysis of accuracy and stability was performed. (iii) A multi-layer target was measured using the point-scanning imaging setup, and the three-dimensional (3D) full-field imaging setup was

verified to confirm the usefulness of the optical Vernier sampling method based on the dual-comb-swept laser.

### A. Measurement of the PSF of the Dual-Comb-Swept Laser

PSF measurement was performed to demonstrate the optical aliasing characteristics and evaluate the improvement in the coherence length of the comb-swept laser compared to the conventional continuous swept laser.

Figure 3 shows the results obtained from the PSF measurement performed using the dual-comb-swept laser. The FFT peak intensity trace was measured along the aliased distance axis while increasing the absolute distance of the target mirror from 1 to 80 mm at increments of 0.4 mm. In the case of the comb A source, increasing the absolute distance from 0 to 3.175 mm shifted the main peak of the FFT peak intensity along the aliased distance axis from 0 to 3.175 mm, as shown in Fig. 3(a). This is called forward correlation. However, when the absolute distance exceeded 3.175 mm, i.e., the principal measurement range (PMR) or  $\Delta d/2$ , the peak position of the FFT intensity shifted to a decreased value for the aliased distance axis, and this is called folded backward correlation. When the absolute distance was 6.350 mm, the aliased distance was 0 mm. This folding phenomenon was repeated with forward and backward correlations at every PMR of each aliasing order [18]. A similar correlation was observed for a PMR of 2.800 mm, as shown in Fig. 3(c) for the corresponding case of the comb B source.

In a general SS-OCT system, the coherence length of the swept-source is defined to have a -6 dB roll-off-length axial position for the continuously decreasing peak values of the FFT intensity starting from the zero-length difference position of the FFT intensity distribution [10]. The coherence length can be newly defined for the comb-swept laser because the aliasing with unexpected back-bounce of the FFT peak intensity is induced by increasing the absolute distance due to the aliasing of the interference subsampling from discrete spectral sweeping. Thus, the coherence length of the comb-swept laser is newly defined by the -6 dB roll-off-length position for decreasing peak values of the FFT intensity at the same aliased distance at every aliasing order. Figures 3(b) and 3(d) show the collection of the first 0.4 mm positions of each forward aliased distance for the 1st to 13th orders of the PSF measurement of combs A and B sources, respectively. In Fig. 3(b), the approximate -6 dB roll-off position corresponds to the 12th order in the comb A source. Similarly, in Fig. 3(d), the approximate -6 dB roll-off point is on the 11th order in the comb B source. Thus, the coherence lengths of combs A and B can be measured to be  $\sim 140$  mm and  $\sim 112$  mm, respectively. The measured coherence lengths of comb A and comb B can be converted to the linewidth of comb A and comb B, which are  $\sim 1.38$  pm and  $\sim 1.84$  pm, respectively [24].

The axial resolution of combs A and B can be represented from the full width at half-maximum (FWHM) of the PSF [24]. Based on the PSF measurement at the absolute distance of 0.4 mm, the measured FWHMs of combs A and B

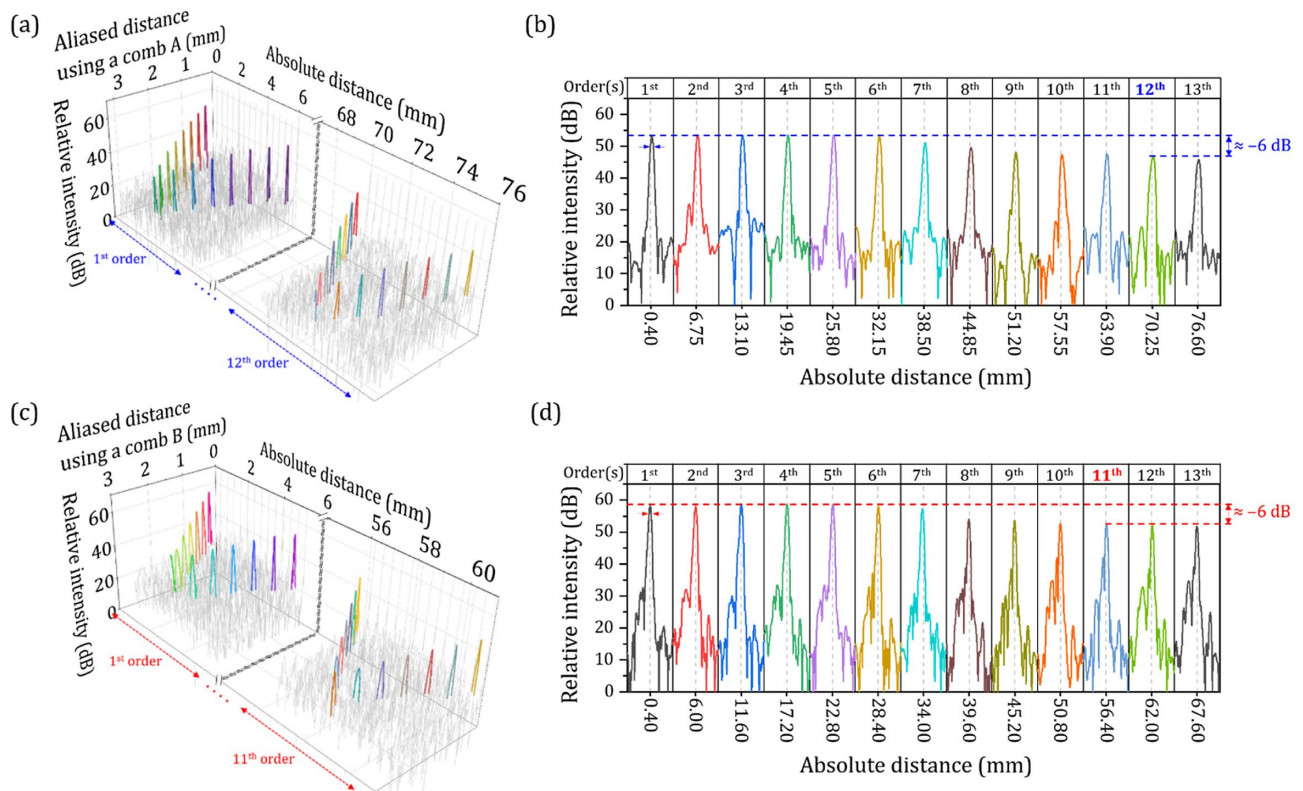


**Fig. 3.** PSF measurements at every 0.4 mm interval using (a) comb A for the 1st and 12th orders and (c) comb B for the 1st and 11th orders. (b) and (d) show the collected first 0.4 mm positions of each forward aliased distance using combs A and B sources, respectively, for the 1st to 13th orders.

[represented by the arrows in Figs. 3(b) and 3(d)] were  $\sim 0.03408$  mm and  $\sim 0.03143$  mm, respectively. So, we estimated the overall resolution of recovered distance will be  $\sim 0.03408$  mm, which is the lower resolution value from combs A and B. Figures 3(a) and 3(b) show the detailed PSF measurement performed at every 0.4 mm interval of absolute distance. The aliasing orders of comb A are the 1st and 12th, and the aliasing orders of comb B are the 1st and 11th. This distance aliasing phenomenon, which depends on the absolute distance, is the main feature of comb-swept lasers employed in optical interferometry. The advantages of comb-swept lasers include an enhanced coherence length of over 100 mm owing to the narrower linewidth achieved when using an etalon and the reduced electrical bandwidth owing to the lower optical frequency for detection [17–19]. However, their main disadvantage has been that an absolute distance cannot be measured, and multiple layers cannot be distinguished when measuring each position because of the distance aliasing. Thus, on the basis of the results obtained in this study, we can conclude that distance aliasing can be solved by the optical Vernier sampling method according to theoretical and experimental investigations.

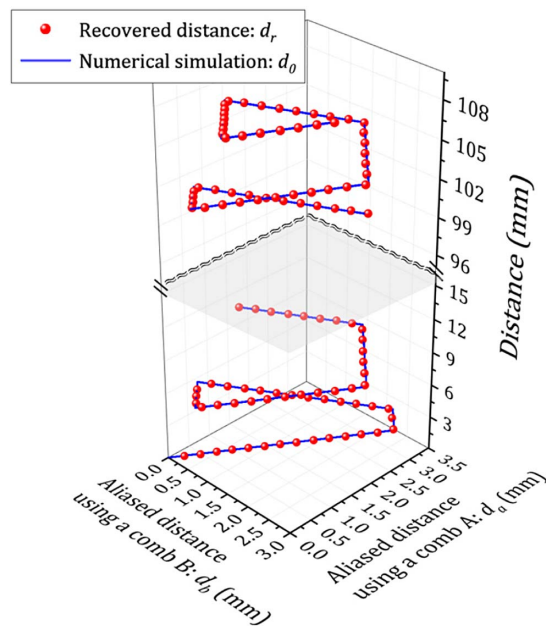


**Fig. 4.** Comparison of the recovered distance measurement with a numerical simulation.

## B. Recovering the Absolute Distance Using the Optical Vernier Sampling Method Compared with Numerical Simulations

To verify our principle for solving distance aliasing, we recovered the absolute distance from a one-to-one correspondence with the ordered pair of two aliased distances using combs A and B in the discrete interval of the absolute distance, as shown in Fig. 4. The absolute distance measurement using the dual-comb-swept laser with combs A and B was performed under the experimental conditions of a 0.2 mm increment for the absolute distance and a 100 mm absolute distance difference for the target mirror.

As shown in Eq. (3), the recovered distance,  $d_r$ , is represented by a bijective functional form that includes the pair  $d_a$  and  $d_b$  with different aliasing orders, namely,  $o_a$  and  $o_b$ . However, in the practical recovery algorithm that incorporates the optical Vernier sampling method, only the aliased distances,  $d_a$  and  $d_b$ , were sufficient for recovering  $d_r$ . Because almost all of the ordered pairs of  $(d_a, d_b)$  indicate a single  $d_r$ , within the coherence length of a given dual-comb-swept laser source, we can ignore few exceptional cases of blind spots where the same ordered pair  $(d_a, d_b)$  indicates multiple recovered distances,  $d_r$ . This is described in detail in Appendix B. Furthermore, the information regarding  $o_a$  and  $o_b$  can be consequently obtained from the confirmed value of the recovered distance,  $d_r$ .

According to the experimental results shown in Fig. 3, the coherence length of the dual-comb-swept laser is more than 100 mm, but the maximum moving range of the translation stage in our laboratory is less than 11 mm. Therefore, the range of the absolute distance measurement was separated into a 0–11 mm region and a 98–109 mm region, and two different translation stages with a separation distance of 100 mm were used. The aliased distances using combs A and B sources are shown by the red filled circles in Fig. 4. Clearly, the ordered pair of the two aliased distances  $(d_a, d_b)$  is sufficient to recover  $d_r$  by one-to-one correspondence for a long range of over 100 mm.

We also compared the recovered distance measured in the discrete interval of the absolute distance with the corresponding values obtained from our numerical simulation. The simulation was performed by combining the theoretical aliasing periods, and the results are represented by the blue solid line in Fig. 4. According to Fig. 4, the recovered distances and numerical simulation according to absolute distance have a similar tendency, and, thus, the proposed method for solving distance aliasing by employing the optical Vernier sampling method works properly over a distance of 100 mm to the target.

Table 1 shows the means and standard deviations (SDs) of distance measurement at four different absolute distances

**Table 1.** Result of Distance Measurement at Four Different Absolute Distances for 100 Times of Repetition (Unit: mm)

	Absolute Distance ( $d_0$ )							
	1		4		7		10	
	Mean	SD	Mean	SD	Mean	SD	Mean	SD
$d_a$	1.012	0.00064	2.343	0.00109	0.679	0.00063	2.675	0.00144
$d_b$	1.017	0.00030	1.588	0.00052	1.441	0.00045	1.164	0.00019
$d_r$	1.015	0.00039	4.009	0.00067	7.035	0.00034	9.997	0.00071



with each 100 data sets. The measurement values (mean  $\pm$  SD) of  $d_r$  were  $1.015 \text{ mm} \pm 0.39 \text{ }\mu\text{m}$ ,  $4.009 \text{ mm} \pm 0.67 \text{ }\mu\text{m}$ ,  $7.035 \text{ mm} \pm 0.34 \text{ }\mu\text{m}$ , and  $9.997 \text{ mm} \pm 0.71 \text{ }\mu\text{m}$ , which confirmed that the optical Vernier sampling method has reliable accuracy and stability.

### C. Multi-Layer Target Measurement Using a Point-Scanning Imaging Setup

Figure 5 shows a multi-layer target measured using a point-scanning imaging setup. A schematic of the point-scanning setup for the multi-layer reflection measurement is shown in Fig. 5(a). Light from the dual-comb-swept laser was divided by OC 1, and the split light traveled toward a delay line (DL) and the multi-layer target through a circulator (CIR). The DL was used to compensate for the optical path difference between the reference light and light reflected from the target layer. The reference light and reflected light were combined in OC 2 and induced the optical interferometric signals from the discrete spectral sweeping light. A balanced detector (BD) was used to suppress the direct current (DC) component of the FFT signal. Figure 5(b) shows an image of the multi-layer target used for this measurement. The multi-layer target was fabricated from an acryl block that was  $50.0 \text{ mm}$  ( $W$ )  $\times$   $50.0 \text{ mm}$  ( $D$ )  $\times$   $51.5 \text{ mm}$  ( $H$ ). The letters P, N, and U with a  $10 \text{ mm}$  depth and a  $3.5 \text{ mm}$  width were carved on the top layer of the block. The absolute distance measurement was performed using the point-scanning setup by utilizing the multi-layer reflections. The region of interest (ROI) was set to  $100 \times 50$  pixels while performing the measurement so that all three letters could be probed. The point-scanning distance interval between each pixel was set to  $0.49 \text{ mm}$ . Thus, the measured area of the ROI was  $49.0 \text{ mm} \times 24.5 \text{ mm}$ . Figure 5(c) shows the result of the physical distance measurement of the multi-layer target after compensation for the refractive index between air and the acryl material. The refractive index of acryl is  $1.5$  in the region around  $800 \text{ nm}$ , and, thus, the recovered distance between the reference and each layer is much longer than the physical distance shown in Fig. 5(d). The recovered distances of layers 3 and 2 are  $83.053 \text{ mm}$  and  $68.186 \text{ mm}$ , respectively. As shown in Eqs. (3) and (A1), the relation between the recovered distance and ordered pair of combs A and B for the three layers can be written as

Layer 1:  $5.950 \text{ mm} = (0.400 \text{ mm}; 1_{\text{odd}}, 0.350 \text{ mm}; 2_{\text{even}})$ ,

Layer 2:  $68.186 \text{ mm} = (1.709 \text{ mm}; 11_{\text{odd}}, 0.986 \text{ mm}; 13_{\text{even}})$ ,

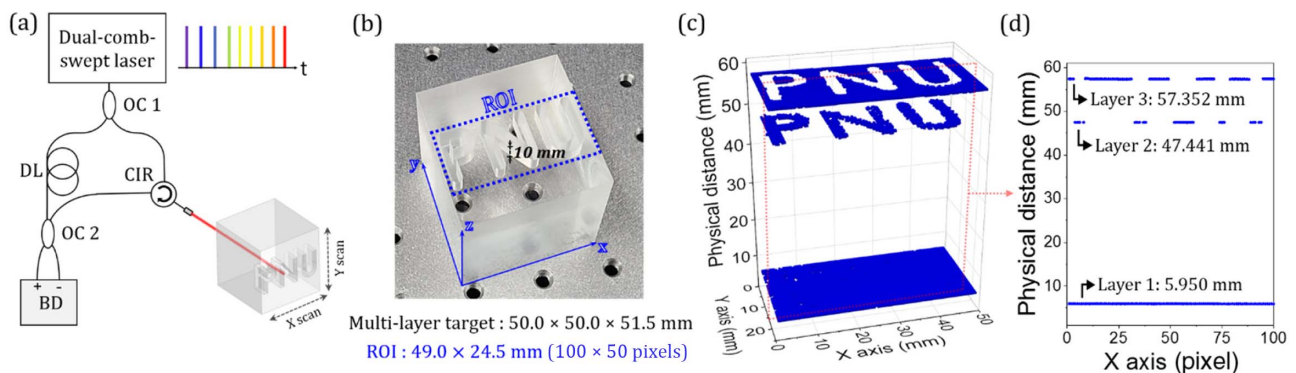
Layer 3:  $83.053 \text{ mm} = (0.503 \text{ mm}; 14_{\text{even}}, 0.947 \text{ mm}; 15_{\text{odd}})$ .

Figure 5(d) shows a cross-sectional view of the result at a transverse position of  $15.68 \text{ mm}$  on the  $Y$  axis (32nd pixel of the  $Y$  axis) and shows the difference between layers. The average physical distances of layers 3, 2, and 1 were  $57.352$ ,  $47.441$ , and  $5.950 \text{ mm}$ , respectively. The difference in the physical distance between layers 3 and 2 was  $9.911 \text{ mm}$ , and the physical distance difference was  $10 \text{ mm}$ . The corresponding physical distance difference between layers 2 and 1 was  $41.491 \text{ mm}$ , and the physical distance difference was  $41.5 \text{ mm}$ . The results shown in Fig. 5 indicate that our solution for distance aliasing using the optical Vernier sampling method was successful for the absolute distance measurement of a multi-layer target with a long-distance difference of over  $83 \text{ mm}$  (corresponding to  $166 \text{ mm}$  of optical-path-length difference).

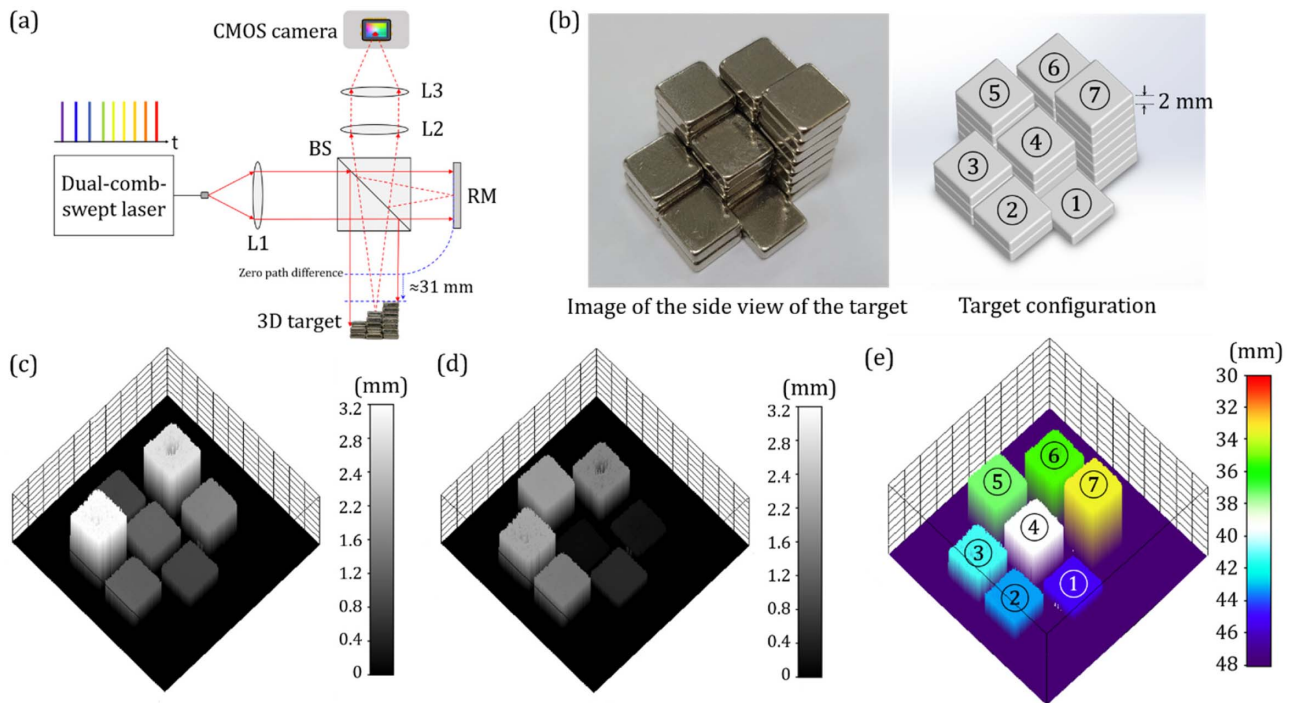
### D. 3D Target Measurement Using a Full-Field Imaging Setup

Figure 6 shows 3D target measurement using a full-field imaging setup. The measurement was performed using a CMOS camera to compensate for the problem of the slow speed of the point-scanning imaging setup shown in Fig. 5. Currently, there are many commercially available high-speed continuous swept lasers that have a repetition rate greater than  $100 \text{ kHz}$  [13,14]. However, the repetition rate of the FFP-TF in our dual-comb-swept laser is limited to a few kHz. Once the CMOS camera took high-speed images at  $335$  frames per second from the high-power area beam of the dual-comb-swept laser, a C-scan of multiple target distances could be taken without beam scanning to improve the imaging speed. In the case of the collection of  $1340$  frames in  $4 \text{ s}$ , the repetition rate of  $0.125 \text{ Hz}$  and  $50\%$  duty ratio are required for dual-comb-swept laser. The total imaging speed is mainly dependent on the performance of the camera because a higher repetition rate (up to  $100 \text{ Hz}$ ) is available to the proposed light source.

Figure 6(a) shows a schematic of the full-field imaging setup. Light from the dual-comb-swept laser passed through



**Fig. 5.** Multi-layer target measurement using a point-scanning setup. (a) Schematic of the point-scanning setup. OC, optical coupler; CIR, circulator; DL, delay line; BD, balanced detector. (b) Image of a multi-layer target. (c) Result of the multi-layer target measurement with refractive index compensation. (d) Cross-sectional view of the result at  $15.68 \text{ mm}$  along the  $Y$  axis (32nd pixel of the  $Y$  axis).



**Fig. 6.** 3D target measurement using a full-field imaging setup. (a) Schematic of the setup. L, lens; BS, beam splitter; RM, reference mirror. (b) Configuration of the 3D targets. Results showing the aliased distance using (c) comb A and (d) comb B sources. (e) Recovered distance data using combs A and B sources based on the optical Vernier sampling method.

lens 1 (L1) and was collimated as an area beam. This beam entered a BS and was split into two paths. One path was toward the 3D target, whereas the other was toward the RM. The light reflected from the RM, and the backscattered light from the 3D target produced an optical interference signal at the BS, which further passed through L2 and L3 and was detected by a specific pixel of the CMOS camera. We used  $500 \times 500$  pixels of the CMOS camera.

An image showing the side view (left) and configuration (right) of the 3D target is presented in Fig. 6(b). The 3D target was assembled with multiple 2-mm-high magnetic blocks. Figures 6(c) and 6(d) show the results of the aliased distance using only comb A or B. The black-and-white scale bars in the figures indicate the aliased distance. Because of distance aliasing, each aliased distance using combs A and B could not measure the recovered distance of the 3D target. The maximum difference in the distance, corresponding to the results shown in Figs. 6(c) and 6(d), was limited to values below the PMR or  $\Delta d/2$ , which were 3.175 and 2.800 mm, respectively. Thus, we could use these two pieces of data from the optical Vernier sampling method to reconstruct the recovered distance and real shape of the target. Figure 6(e) shows the solving of distance aliasing that was successfully recovered by combining the results of combs A and B. The color scale bar indicates a range of 31–47 mm because the 3D target was intentionally located with an offset distance of  $\sim 31$  mm to demonstrate the merit of a long coherence length.

According to Eq. (A1), each surface of recovered distance can be represented as follows:

$$\text{Surface ①: } 45.294 \text{ mm} = (0.844 \text{ mm}; 8_{\text{even}}, 0.494 \text{ mm}; 9_{\text{even}}),$$

$$\text{Surface ②: } 43.271 \text{ mm} = (1.179 \text{ mm}; 7_{\text{odd}}, 1.529 \text{ mm}; 8_{\text{odd}}),$$

$$\text{Surface ③: } 41.290 \text{ mm} = (3.160 \text{ mm}; 7_{\text{odd}}, 2.090 \text{ mm}; 8_{\text{even}}),$$

$$\text{Surface ④: } 39.334 \text{ mm} = (1.234 \text{ mm}; 7_{\text{even}}, 0.134 \text{ mm}; 8_{\text{even}}),$$

$$\text{Surface ⑤: } 37.260 \text{ mm} = (0.840 \text{ mm}; 6_{\text{odd}}, 1.940 \text{ mm}; 7_{\text{odd}}),$$

$$\text{Surface ⑥: } 35.259 \text{ mm} = (2.841 \text{ mm}; 6_{\text{odd}}, 1.659 \text{ mm}; 7_{\text{even}}),$$

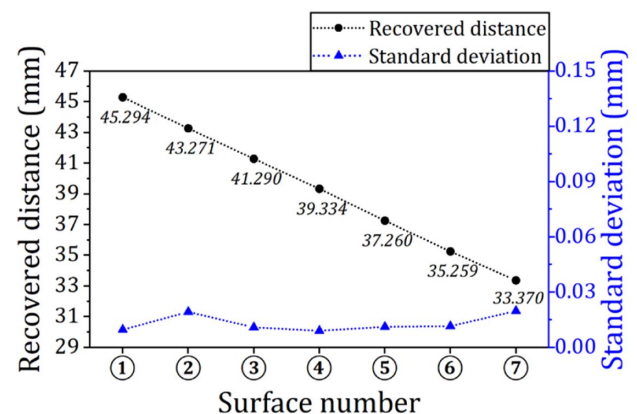


**Fig. 7.** Recovered distance and SD obtained in the 3D target measurement using the full-field setup.



Surface ⑦: 33.370 mm = (1.620 mm;  $6_{\text{even}}$ , 0.230 mm;  $6_{\text{odd}}$ ).

For quantitative analysis of the data in Fig. 6(e), the statistics of the average recovered distance and its SD for each surface (①–⑦) were calculated. Because each magnetic block surface has a height difference of 2 mm, the black filled circles plotted in Fig. 7 show a regular distance interval of 2 mm. As plotted with blue filled triangles in Fig. 7, the SD for each surface represents a much larger value compared to the stability of our system (as shown in Table 1). Therefore, it was considered as the roughness of target surface area. Its maximum value was 0.0197 mm for surface ⑦, whereas its minimum value was 0.0090 mm for surface ④. These values are reasonably small considering the sampling number and environmental conditions.

#### 4. CONCLUSION

In this work, we demonstrated the dual-comb-swept laser for solving distance aliasing using the novel optical Vernier sampling method for the first time, to the best of our knowledge. Similar to the principle of using a Vernier caliper for measuring the length of an object, the optical Vernier sampling method also uses two different frequencies of interferometric signals from a dual-comb-swept laser, which correspond to the different intervals of the two rulers in a Vernier caliper.

According to two different designed FSRs of combs A and B of 47.5 pm (23.7 GHz) and 58.1 pm (26.8 GHz), the corresponding PMR values of 3.175 and 2.800 mm, respectively, were determined. The combination of the two aliased distances below these PMR limits can be used to obtain the recovered distance by solving the distance aliasing using the optical Vernier sampling method. We also measured the recovered distances of three layers separated over 83 mm using the point-scanning imaging setup. The simultaneous absolute distance of the top surfaces separated over 45 mm is also measured using the full-field imaging setup. The key advantage of optical Vernier sampling is data compression in the long range. In the multi-layer target, a recovered distance of 83 mm has data compression rates of 14 times using comb A and 15 times using comb B. In the 3D target, a recovered distance of 45 mm has data compression rates of 8 times using comb A and 9 times using comb B.

On the basis of these results, we expect to expand the application of solving distance aliasing by employing the novel optical Vernier sampling method in systems, such as the highly efficient SS-OCT imaging system, that exhibit an enhanced coherence length for deeper imaging and reduced subsampling frequency for a decreased electrical bandwidth.

#### APPENDIX A: DETAILED DESCRIPTION OF THE DISTANCE EQUATION

From Eq. (3), the recovered distance,  $d_r$ , in the optical Vernier sampling method can be represented in detail as a bijective function as follows:

$$d_r = (d_a; o_{a(\text{even or odd})}, d_b; o_{b(\text{even or odd})}), \quad (\text{A1})$$

where  $d_r$ ,  $d_a$ ,  $o_{a(\text{even or odd})}$ ,  $d_b$ , and  $o_{b(\text{even or odd})}$  represent the recovered distance, aliased distance using comb A, aliasing order using comb A, aliased distance using comb B, and aliasing

#### Absolute distance recovery algorithm

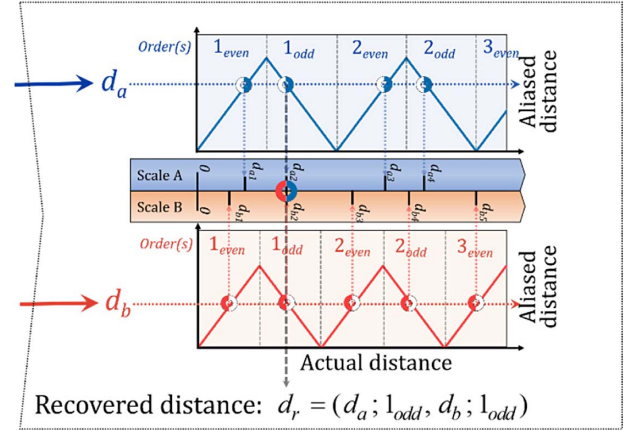


Fig. 8. Schematic showing the use of the recovery algorithm to obtain the recovered distance.

order using comb B. Thus, it is possible to show that the recovered distance consists of the abovementioned four measured factors for combs A and B together using a single correspondence expression, as given by Eq. (A1). Figure 8 shows the schematic depiction of the use of the recovery algorithm for obtaining the recovered distance,  $d_r$ . The main difference between Figs. 1 and 8 is the axis conversion from the frequency scale to the distance scale using Eq. (1). Each aliasing order of comb A and comb B is divided into even and odd orders, respectively. Each even order has a forward correlation, whereas each odd order has a backward correlation between the actual and aliased distances for combs A and B. To numerically display a bijective function of  $d_r$ , we used a well-known definition of the greatest integer function (floor function), as expressed by

$$\lfloor x \rfloor = \max\{n \in \mathbb{Z} : n \leq x\}, \quad (\text{A2})$$

where  $\lfloor x \rfloor$  of a real number  $x$  denotes the greatest integer less than or equal to  $x$ . For example,  $\lfloor 0.1 \rfloor = 0$ ,  $\lfloor 9.966 \rfloor = 9$ ,  $\lfloor 3.5 \rfloor = 3$ , and  $\lfloor -\pi \rfloor = -4$ .

Each element in Eq. (A1) can be defined using Eqs. (A3) and (A4) where  $\text{PMR}_a$  and  $\text{PMR}_b$  represent PMR when using combs A and B, respectively:

$$\left. \begin{aligned} d_a &= \text{PMR}_a \times \left( \frac{d_r}{\text{PMR}_a} - \left\lfloor \frac{d_r}{\text{PMR}_a} \right\rfloor \right), \\ o_{a(\text{even})} &= \left\lfloor \frac{d_r}{2 \times \text{PMR}_a} + 1 \right\rfloor, \end{aligned} \right\} \quad \text{when } \left\lfloor \frac{d_r}{\text{PMR}_a} \right\rfloor = \text{even number},$$

$$\left. \begin{aligned} d_a &= \text{PMR}_a - \text{PMR}_a \times \left( \frac{d_r}{\text{PMR}_a} - \left\lfloor \frac{d_r}{\text{PMR}_a} \right\rfloor \right), \\ o_{a(\text{odd})} &= \left\lfloor \frac{d_r}{2 \times \text{PMR}_a} + 1 \right\rfloor, \end{aligned} \right\} \quad \text{when } \left\lfloor \frac{d_r}{\text{PMR}_a} \right\rfloor = \text{odd number}, \quad (\text{A3})$$

$$\left. \begin{aligned} d_b &= \text{PMR}_b \times \left( \frac{d_r}{\text{PMR}_b} - \left\lfloor \frac{d_r}{\text{PMR}_b} \right\rfloor \right), \\ o_{b(\text{even})} &= \left\lfloor \frac{d_r}{2 \times \text{PMR}_b} + 1 \right\rfloor, \end{aligned} \right\} \\
 \text{when } \left\lfloor \frac{d_r}{\text{PMR}_b} \right\rfloor = \text{even number}, \\
 \left. \begin{aligned} d_b &= \text{PMR}_b - \text{PMR}_b \times \left( \frac{d_r}{\text{PMR}_b} - \left\lfloor \frac{d_r}{\text{PMR}_b} \right\rfloor \right), \\ o_{b(\text{odd})} &= \left\lfloor \frac{d_r}{2 \times \text{PMR}_b} + 1 \right\rfloor, \end{aligned} \right\} \\
 \text{when } \left\lfloor \frac{d_r}{\text{PMR}_b} \right\rfloor = \text{odd number.} \quad (\text{A4})$$

Using these two sets of equations, all of the recovered distances can be bijectively correlated to the factors in Eq. (A1). In the practical recovery algorithm that incorporates the optical Vernier sampling method, only the aliased distances using combs A and B are sufficient for recovering the absolute distance. The order can be consequently obtained via the confirmed value of the recovered distance.

## APPENDIX B: SOLUTIONS FOR A BLIND SPOT

Most of the recovered distances,  $d_r$ , were matched by a one-to-one correspondence with the ordered pair of two aliased distances,  $(d_a, d_b)$ , using combs A and B. However, a few exceptional cases still exist because of the folded backward correlation. For example, for an absolute distance movement below 10 mm, six positions of blind spots exist when multiple recovered distances,  $d_r$ , correspond to the same combination pair of  $(d_a, d_b)$ . In our practical measurement system, the blind spots can be easily solved using a specific algorithm for the reference movement, as shown in Fig. 9.

Target measurement using optical Vernier sampling was conducted using the dual-comb-swept laser, and the aliased distance pair  $(d_a, d_b)$  was made. When the aliased distance pair  $(d_a, d_b)$  indicates a single recovered distance,  $d_r$ , the latter can be used directly without further action. However, if the aliased distance  $(d_a, d_b)$  corresponds to multiple cases of the recovered distance,  $d_r$ , the RM is required to be shifted slightly to remeasure the newly ordered pairs. In this case, the newly aliased distance pair using combs A and B is represented by  $(d'_a, d'_b)$ , which indicates the newly recovered distance,  $d'_r$ . By rescaling  $d'_r$  with the new movement distance of the RM, we can obtain a single recovered distance,  $d_r$ .

There is a fundamental solution to ultimately remove blind spots. Because the confusion of multiple  $d_r$  for the same pairs of  $(d_a, d_b)$  arises from the folded backward correlation, this problem can be solved by leaving only the forward correlation, which is possible when using the optical in-phase/quadrature (I/Q) demodulation and frequency shifting techniques [11,25,26]. Therefore, theoretically, the recovered distance can be extended up to a much longer length of the least common multiple (LCM) of the two values of the PMR of both combs A and B. As shown in Fig. 10, the numerical simulation result is plotted without the folded backward correlation. We assume that the PMR of comb A doubles to 6.350 mm and that of comb B becomes 5.600 mm. Unlike Fig. 4, most of the lines

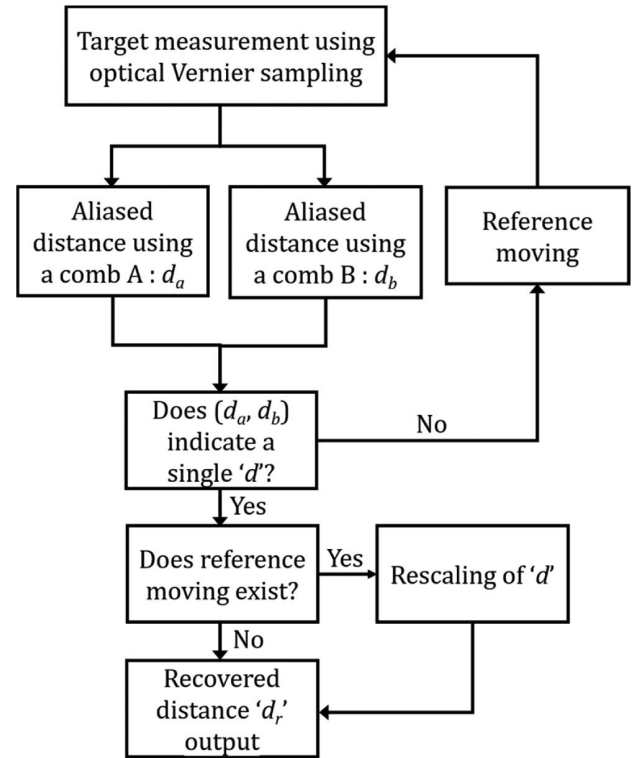


**Fig. 9.** Flowchart for the reference movement to solve the blind spot problem.

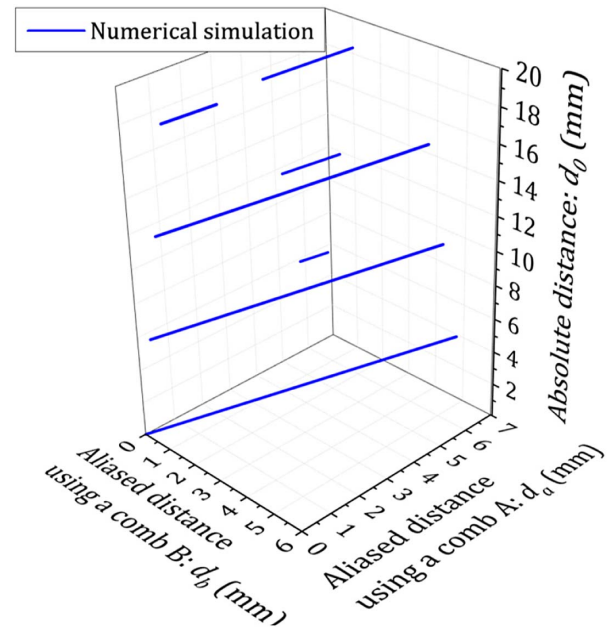


**Fig. 10.** Results of the numerical simulation employing the I/Q demodulation and frequency shifter.

in Fig. 10 are parallel to each other along the absolute distance up to 20 mm, and clearly, there is no folding line that can give rise to duplicated positions.

**Funding.** Korea Medical Device Development Fund grant funded by the Korea government (the Ministry of Science and ICT, the Ministry of Trade, Industry and Energy, the Ministry of Health and Welfare, the Ministry of Food and Drug Safety) (202011C13, KMDF\_PR\_20200901\_0055); Commercialization Promotion Agency for R&D Outcomes (COMPA) funded by the Ministry of Science and ICT (1711123345); Korea Institute for Advancement of Technology (KIAT) grant funded by the Ministry of Trade, Industry and Energy (N0002310).

**Disclosures.** The authors declare no conflicts of interest.

<sup>†</sup>These authors contributed equally to this work.

## REFERENCES

- D. Huang, F. Li, C. Shang, Z. Cheng, S. T. Chu, and P. K. A. Wai, "Frequency comb swept laser with a high-Q microring filter," *Photon. Res.* **8**, 904–911 (2020).
- J. Jerwick, Y. Huang, Z. Dong, A. Sladades, A. J. Brucker, and C. Zhou, "Wide-field ophthalmic space-division multiplexing optical coherence tomography," *Photon. Res.* **8**, 539–547 (2020).
- X. Zhang, J. Pouls, and M. C. Wu, "Laser frequency sweep linearization by iterative learning pre-distortion for FMCW LiDAR," *Opt. Express* **27**, 9965–9974 (2019).
- H. D. Lee, M. Y. Jeong, C. S. Kim, J. G. Shin, B. H. Lee, and T. J. Eom, "Linearly wavenumber-swept active mode locking short-cavity fiber laser for *in-vivo* OCT imaging," *IEEE J. Sel. Top. Quantum Electron.* **20**, 1101008 (2014).
- M. Siddiqui and B. J. Vakoc, "Optical-domain subsampling for data efficient depth ranging in Fourier-domain optical coherence tomography," *Opt. Express* **20**, 17938–17951 (2012).
- J. Cao, P. Wang, Y. Zhang, G. Shi, B. Wu, S. Zhang, and Y. Liu, "Methods to improve the performance of the swept source at 10  $\mu\text{m}$  based on a polygon scanner," *Photon. Res.* **5**, 245–250 (2017).
- F. Hou, M. Zhang, Y. Zheng, L. Ding, X. Tang, and Y. Liang, "Detection of laser-induced bulk damage in optical crystals by swept-source optical coherence tomography," *Opt. Express* **27**, 3698–3709 (2019).
- R. Su, M. Kirillin, E. W. Chang, E. Sergeeva, S. H. Yun, and L. Mattsson, "Perspectives of mid-infrared optical coherence tomography for inspection and micrometrology of industrial ceramics," *Opt. Express* **22**, 15804–15819 (2014).
- N. Lippok, M. Siddiqui, B. J. Vakoc, and B. E. Bouma, "Extended coherence length and depth ranging using a Fourier-domain mode-locked frequency comb and circular interferometric ranging," *Phys. Rev. Appl.* **11**, 014018 (2019).
- H. D. Lee, G. H. Kim, J. G. Shin, B. Lee, C. S. Kim, and T. J. Eom, "Akinetic swept-source optical coherence tomography based on a pulse-modulated active mode locking fiber laser for human retinal imaging," *Sci. Rep.* **8**, 17660 (2018).
- M. Siddiqui, A. S. Nam, S. Tozburun, N. Lippok, C. Blatter, and B. J. Vakoc, "High-speed optical coherence tomography by circular interferometric ranging," *Nat. Photonics* **12**, 111–116 (2018).
- T. S. Kim, J. Y. Joo, I. Shin, P. Shin, W. J. Kang, B. J. Vakoc, and W. Y. Oh, "9.4 MHz A-line rate optical coherence tomography at 1300 nm using a wavelength-swept laser based on stretched-pulse active mode-locking," *Sci. Rep.* **10**, 9328 (2020).
- Z. Wang, B. Potsaid, L. Chen, C. Doerr, H.-C. Lee, T. Nielson, V. Jayaraman, A. E. Cable, E. Swanson, and J. G. Fujimoto, "Cubic meter volume optical coherence tomography," *Optica* **3**, 1496–1503 (2016).
- D. Huang, F. Li, C. Shang, Z. Cheng, and P. K. A. Wai, "Reconfigurable time-stretched swept laser source with up to 100 MHz sweep rate, 100 nm bandwidth, and 100 mm OCT imaging range," *Photon. Res.* **8**, 1360–1367 (2020).
- J. P. Kolb, W. Draxinger, J. Klee, T. Pfeiffer, M. Eibl, T. Klein, W. Wieser, and R. Huber, "Live video rate volumetric OCT imaging of the retina with multi-MHz A-scan rates," *PLoS ONE* **14**, e0213144 (2019).
- S. Bak, G. H. Kim, and C. S. Kim, "Dual-band wavelength-comb-swept laser to extend displacement measurement range," in *European Conference on Biomedical Optics* (2019), paper 11078\_67.
- E. J. Jung, J.-S. Park, M. Y. Jeong, C.-S. Kim, T. J. Eom, B.-A. Yu, S. Gee, J. Lee, and M. K. Kim, "Spectrally-sampled OCT for sensitivity improvement from limited optical power," *Opt. Express* **16**, 17457–17467 (2008).
- S.-K. Chun, H. Jang, S.-W. Cho, N. S. Park, and C.-S. Kim, "Unfolding displacement measurement method for the aliasing interferometer signal of a wavelength-comb-swept laser," *Opt. Express* **26**, 5789–5799 (2018).
- N. S. Park, S. K. Chun, G. H. Han, and C. S. Kim, "Acousto-optic-based wavelength-comb-swept laser for extended displacement measurements," *Sensors* **17**, 140 (2017).
- G. Berkovic and E. Shafir, "Optical methods for distance and displacement measurements," *Adv. Opt. Photon.* **4**, 441–471 (2012).
- T.-H. Tsai, C. Zhou, D. C. Adler, and J. G. Fujimoto, "Frequency comb swept lasers," *Opt. Express* **17**, 21257–21270 (2009).
- N. Lippok and B. J. Vakoc, "Resolving absolute depth in circular-ranging optical coherence tomography by using a degenerate frequency comb," *Opt. Lett.* **45**, 371–374 (2020).
- A. D. Gomes, M. S. Ferreira, J. Bierlich, J. Kobelke, M. Rothhardt, H. Bartelt, and O. Frazão, "Optical harmonic Vernier effect: a new tool for high performance interferometric fibre sensors," *Sensors* **19**, 5431 (2019).
- W. Drexler and J. G. Fujimoto, *Optical Coherence Tomography: Technology and Applications* (Springer, 2015).
- S. H. Yun, G. J. Tearney, J. F. de Boer, and B. E. Bouma, "Removing the depth-degeneracy in optical frequency domain imaging with frequency shifting," *Opt. Express* **12**, 4822–4828 (2004).
- M. Siddiqui, S. Tozburun, E. Z. Zhang, and B. J. Vakoc, "Compensation of spectral and RF errors in swept-source OCT for high extinction complex demodulation," *Opt. Express* **23**, 5508–5520 (2015).